JOURNAL OF GUIDANCE, CONTROL, AND DYNAMICS
Vol. 33, No. 3, May–June 2010

Reachable and Controllable Sets for Planetary Entry and Landing

Joel Benito* and Kenneth D. Mease†
University of California, Irvine, Irvine, California 92697-3975

DOI: 10.2514/1.47577

Understanding the envelope of entry trajectories that a given planetary lander is capable of flying can be an important aid for mission analysis and design. Two characteristics of this envelope are considered: 1) the set of states reachable from a given entry state and 2) the set of entry states controllable to a given final state. Precise definitions of these sets are given and methods for computing them are presented. To illustrate their use, the sets are employed to characterize the performance of two vehicle configurations, a low lift-to-drag-ratio capsule and a mid lift-to-drag-ratio ellipsled, for Mars entry. Roles for the sets in evaluating entry trajectory planning algorithms, choosing a nominal entry state, and planning skip entries are described.

Nomenclature

CFP	=	controllable set footprint
CS	=	controllable set
C_D	=	drag coefficient
C_L	=	lift coefficient
C_γ	=	component of the Coriolis acceleration in the flight-path-angle equation
C_ψ	=	component of the Coriolis acceleration in the heading-angle equation
D	=	drag acceleration
F	=	set of feasible control-trajectory pairs
g	=	gravitational acceleration
h	=	altitude
h_s	=	atmospheric density scale height
J	=	cost function
k_q	=	stagnation point convective heat rate constant
L	=	lift acceleration
m	=	vehicle mass
P	=	set of states that do not violate path constraints
Q	=	stagnation point convective heat load
$\dot{Q}$	=	stagnation point convective heat rate
$\bar{q}$	=	dynamic pressure
RFP	=	reachable set footprint
RS	=	reachable set
r	=	distance from planet's center to the vehicle's center of mass
r_n	=	nose radius
S	=	reference surface
T	=	transition map
U	=	set of admissible control profiles
V	=	velocity
V_s	=	speed of sound
γ	=	flight-path angle
Δ	=	set of allowable deployment states
θ	=	longitude
μ	=	planet's gravitational constant
Π	=	longitude and latitude extraction map
ρ	=	atmospheric density
ρ_0	=	sea-level atmospheric density
σ	=	bank angle
ϕ	=	latitude
X	=	set of allowable states
ψ	=	heading angle
ω_p	=	planet rotation rate
:	=	such that (when used in set notation)
$\subset$	=	is a subset of
$\in$	=	is an element of
$\forall$	=	for all
$\exists$	=	there exists
$\cup$	=	set union

Subscripts

0	=	initial
f	=	final
(θ, ϕ)	=	restricted to the particular value of the (θ, ϕ) pair

Superscript

J	=	minimizes the cost function J

I. Introduction

FOR planetary landing mission analysis and design, it is beneficial to characterize the envelope of trajectories that a given lander is capable of flying. In this paper, two characteristics of this envelope are the focus of attention: 1) the reachable set: the set of parachute-deployment states reachable from a given entry state; and 2) the controllable set: the set of entry states controllable to a given final state. The objectives of this paper are to define the reachable set (RS) and the controllable set (CS), to present methods for their computation, to illustrate their use in assessing the performance of two vehicle configurations for Mars entry, and to identify several other uses for the sets.

Reachable and controllable sets are established concepts in mathematical systems theory; see for example [1]. The standard definitions are adapted to accommodate the particular features of entry flight: the boundary conditions and the path and control constraints. The landing footprint, a more familiar concept in flight mechanics, can be derived from the reachable set. The landing footprint is a two-dimensional set, typically given in terms of longitude and latitude. See [2] for an early paper describing landing footprints, [3] for optimal landing footprints, and [4] for a fast suboptimal computational approach. The RS is a six-dimensional set of values for the translational state variables of the entry vehicle. Using spherical coordinates for position and velocity, the state variables are radius, longitude, latitude, velocity, flight-path angle, and heading angle. The landing footprint is, in a sense, a projection of the RS onto the longitude–latitude plane, and to emphasize this connection we use the term reachable set footprint (RFP). Keeping track of the full translational state for the points that can be reached by

Received 9 October 2009; revision received 19 January 2010; accepted for publication 24 January 2010.

*Graduate Student, Mechanical and Aerospace Engineering; jbenitom@uci.edu.

†Professor, Mechanical and Aerospace Engineering; kmease@uci.edu. Associate Fellow AIAA.

a lander is important when state variables in addition to longitude and latitude are of interest. For example, there may be multiple points in the RS with the same longitude and latitude, and the one of most interest might be the one with the highest altitude.

The controllable set can be viewed as a generalization of the entry corridor. The entry corridor is typically defined as the one-dimensional set of the allowable entry flight-path angles [2]. The determination of the entry corridor is important for mission planning and design, and it is in the list of recommendations for the design of entry guidance systems in [5]. A study of the effect of lift on the entry corridor is presented in [6]. The steepest entry flight-path angle is typically dictated by a thermal or structural vehicle constraint. The shallowest entry flight-path angle typically corresponds to a trajectory on the verge of skipping out of the atmosphere. A two-dimensional version of the entry corridor has also been defined to show the variation of the allowable entry flight-path-angle range with entry velocity as in [7] for Mars aerocapture. The CS includes points parameterized by all the longitudinal and lateral state variables; thus, it is a set in the six-dimensional state space. The CS provides a complete representation of the entry states from which a vehicle can reach a given landing site. The projection of the CS in the latitude–longitude plane is the controllable set footprint (CFP).

Figures 1 and 2 illustrate the RS and CS and their corresponding footprints in three dimensions, though the sets actually include the velocity variables and are six-dimensional.

Computing the complete reachable and controllable sets or even just their boundaries would be computationally intensive. Instead, certain extremal points in the sets that are of most interest are computed. Extreme values of quantities are displayed for the reachable and controllable longitude–latitude pairs. A scoring function is used to summarize all the trajectory characteristics and identify preferred areas within the reachable and controllable sets for placing the nominal landing and entry states, respectively.

To illustrate the computation and use of these sets, the RS and CS are obtained for a representative Mars entry mission. Certain future Mars missions are pushing entry, descent, and landing technology to achieve more accurate and higher-elevation landings [7]. To date, Mars landings have been at sites below −1.4 km Mars orbiter laser altimeter (MOLA) elevation. To reach much of the Ancient Highlands, the majority of the southern hemisphere, landing at +2 km MOLA elevations is required. All previous missions to Mars have had unguided entries with landing errors only guaranteed to be on the order of 100 km. The Mars Science Laboratory (MSL) lander will have a guided entry designed to land within 10 km of the desired site. High-elevation landing sites are especially challenging because the parachute-deployment altitude has to be higher also. Although there exist nominal trajectories that meet the requirements, if they involve lofting in the final entry phase, the amount of lift available to compensate for off-nominal conditions may be less than needed. Some algorithms have been developed [8,9] to provide reference trajectories that preserve control authority to correct for errors during the final entry phase. An alternative vehicle configuration for this type of mission is an ellipsled, which has a higher lift-to-drag ratio (L/D) compared with that of a capsule. The RS and CS for Mars entry will be characterized for these two vehicle configurations to assess the impact of L/D on the entry capability with regard to parachute-deployment altitude, landing footprint, feasibility in the entry targeting, and heat rate and load.

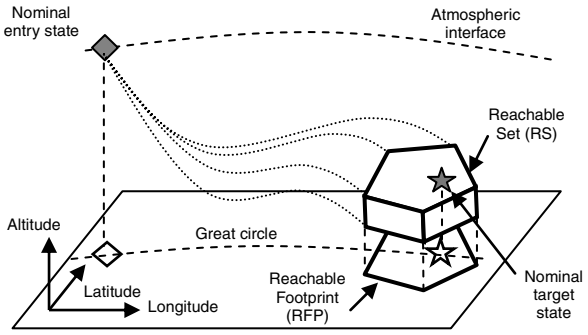

Fig. 1 Reachable set and reachable footprint.

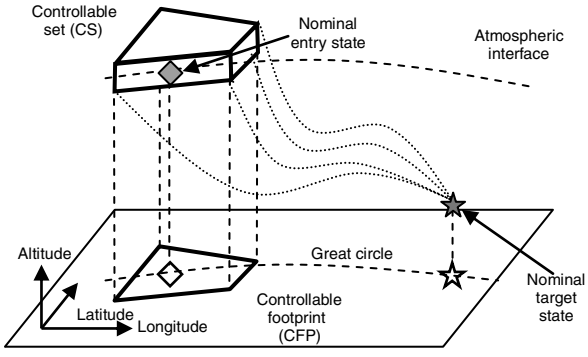

Fig. 2 Controllable set and controllable footprint.

II. Entry Problem Formulation

A. Equations of Motion

The equations of motion of an entry vehicle defined with respect to a planet-fixed coordinate frame are [3]

$$\dot{r} = V\sin\gamma \qquad \dot{\theta} = \frac{V}{r}\frac{\cos\gamma\cos\psi}{\cos\phi} \qquad \dot{\phi} = \frac{V}{r}\cos\gamma\sin\psi$$

$$\dot{V} = -D - g\sin\gamma \qquad \dot{\gamma} = \frac{1}{V}\left[L\cos\sigma - \left(g - \frac{V^2}{r}\right)\cos\gamma\right] + C_\gamma$$

$$\dot{\psi} = -\frac{1}{V\cos\gamma}\left(L\sin\sigma + \frac{V^2}{r}\cos^2\gamma\cos\psi\tan\phi\right) + C_\psi \tag{1}$$

where θ is the longitude, ϕ is the latitude, r is the distance from the center of the planet to the vehicle center of mass, ψ is the heading angle with $\psi = 0$ as due east and $\psi = 90$ deg as due north, V is the velocity, and γ is the flight-path angle. The bank angle is σ, the angle the lift vector is rotated around the velocity axis, with $\sigma = 0$ corresponding to vertical upward and positive σ generating a right turn. L and D are the lift and drag accelerations, defined by

$$L = \frac{1}{2}\rho V^2\frac{S}{m}C_L \qquad D = \frac{1}{2}\rho V^2\frac{S}{m}C_D \tag{2}$$

The drag and lift coefficients C_D and C_L are solely functions of the Mach number. Angle of attack is not considered a controllable variable; it takes a Mach-number-dependent trim value dictated by the vehicle's aerodynamics. S is the reference area, m is the vehicle mass, and ρ is the atmospheric density. g is the gravitational acceleration. The terms C_ψ and C_γ are the Coriolis acceleration components due to planet rotation and can be approximated by

$$C_\gamma = 2\omega_p\cos\psi\cos\phi \qquad C_\psi = 2\omega_p(\tan\gamma\sin\psi\cos\phi - \sin\phi) \tag{3}$$

where ω_p is the planet angular rotation rate.

B. Downrange, Crossrange, and Control Authority Definitions

Distances traveled on the surface of the planet are measured with respect to the great circle arc that includes the projection of nominal entry and target points on the surface of the planet (see Fig. 3). The traveled distance parallel to the great circle arc is the downrange, and the perpendicular distance is the crossrange. Positive crossranges correspond to positions on the starboard side of the great circle arc and negative crossranges correspond to positions on the port side.

As explained in the Introduction, for the mission studied it is of special interest to deploy the parachute at high altitudes, although always within the allowable ranges of deployment dynamic pressure and Mach number dictated by the parachute requirements. These limits will be given in Sec. II.E. The challenge of high-altitude parachute deployment is the decreased atmospheric density, which

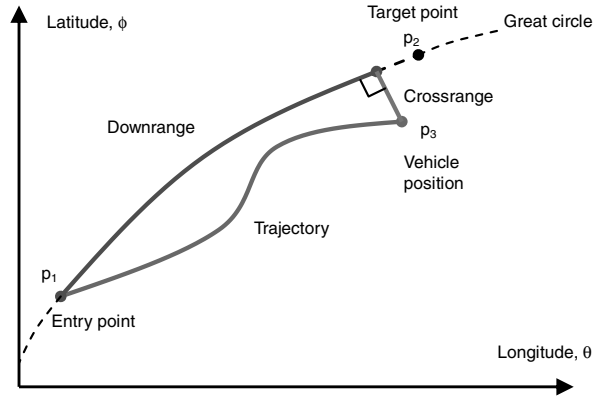

Fig. 3 Trajectory metrics.

implies low control authority due to less lift. The altitude vertical acceleration is

$$\ddot{h} = -g - D\sin\gamma + \frac{V^2}{r}\cos^2\gamma + L\cos\gamma\cos\sigma + V\cos\gamma C_\gamma \quad (4)$$

The term $L\cos\gamma$ is referred to as the altitude control authority (see [10] for a related definition). Especially close to the deployment point when the velocity is low, it is important to have as much altitude control authority as possible. $L\cos\gamma$ can be increased in different ways, although they all effectively limit lofting motion near the end of entry, because lofting decreases both L and $\cos\gamma$. This issue is further considered in Secs. IV and V.

C. Vehicle Model

The geometry of an MSL-type capsule [11] is a double-cone, with an aeroshell forebody shape of a 70 deg sphere-cone. This configuration can provide a maximum L/D of about 0.25. An alternative configuration is the ellipsled vehicle [10,11]. The ellipsled geometry is an elliptically blunted cylinder. This configuration can provide an L/D as high as 0.4. Figure 4 shows sketches of the MSL and ellipsled configurations.

The constraints described in the remainder of this subsection apply to both vehicle configurations. Bank angle, the means of flight-path control, is limited to $|\sigma| \leq 120$ deg. Because of limitations in the reaction control system, the bank rate and bank accelerations are limited to $|\dot{\sigma}| \leq 20$ deg/s and $|\ddot{\sigma}| \leq 5$ deg/s^2. The vehicle has constraints on acceleration, dynamic pressure, heat rate, and heat load. These constraints will not be imposed in the computations, but the values of those variables will be considered. Convective heat rate $\dot{Q}$ can be approximated at the stagnation point by the Sutton–Graves equation [12]:

$$\dot{Q} = k_q\left(\frac{\rho}{r_n}\right)^N V^M \quad (5)$$

where $N = 0.5$, $M = 3$, $k_q = 1.9027\text{e}-4$, ρ is the atmospheric density, and r_n is the vehicle nose radius. The total heat load Q absorbed at the stagnation point of the vehicle is the time integral of the heat rate. Dynamic pressure $\bar{q}$ is given by

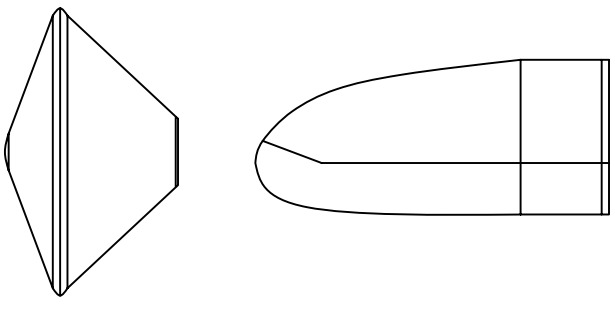

Fig. 4 MSL and ellipsled configurations.

Table 1 Vehicle parameters

	MSL-type	Ellipsled	Units
C_D	1.45	1.92	-
C_L	0.36	0.62	-
L/D	0.248	0.323	-
m	2804	2804	kg
S	15.9	15.9	m^2
r_n	0.66	0.66	m

Table 2 Martian parameters

Parameter	Value	Units
r_p	3.3866e6	m
μ	4.284e13	m^3/s^2
ρ_0	0.0158	kg/m^3
h_s	9354.5	m
V_s	220	m/s
ω_p	7.095e − 5	rad/s

$$\bar{q} = \frac{1}{2}\rho V^2 \quad (6)$$

For the results in this paper the lift and drag coefficients are assumed to be constant, a standard approximation for the hypersonic regime. The parameters of the vehicles used in the simulations are shown in Table 1 and are representative of the geometries chosen. Note that the mass, reference surface, and nose radius are taken to be the same for both vehicles, in order to study the effect of L/D alone.

D. Atmospheric and Planetary Models

The atmospheric density ρ is approximated by the exponential function

$$\rho = \rho_0 \exp(-h/h_s) \quad (7)$$

where ρ_0 is the density on the surface of the planet, h is the altitude, and h_s is the density scale height. The planet is assumed to be spherical with a surface radius r_p, and hence $h = r - r_p$. Given that in this paper the aerodynamic coefficients are assumed constant, the speed of sound is only needed for the definition of the parachute constraints. For the range of low altitudes involved, the speed of sound can be modeled by a constant velocity V_s. The gravitational acceleration is modeled by $g = \mu/r^2$, where μ is the planet gravitational constant. The values of the Martian parameters used in the computations are shown in Table 2.

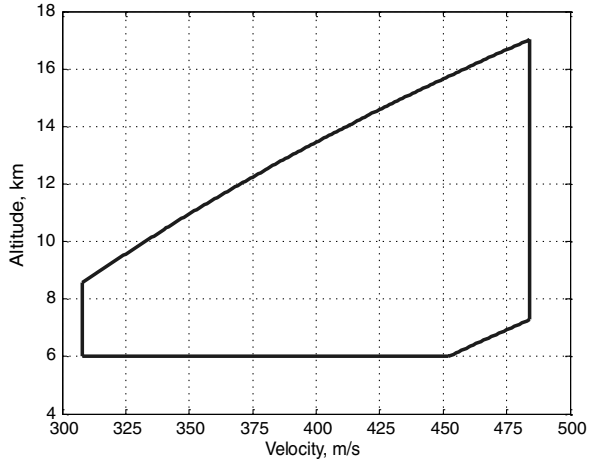

Fig. 5 Disk-gap-band parachute box.

E. Parachute Deployment Constraints

To date, the parachute technology used for Mars landers is that inherited from the Viking program [7]. The selected parachute configuration is the disk-gap band, which must be deployed in the dynamic pressure range of 300–850 Pa and the Mach number range of 1.4–2.2. The minimum deployment altitude is set to 6 km. When converted to altitude-velocity constraints, for a given atmospheric model, the parachute box, or set of all allowable deployment altitude-velocity pairs, is as shown in Fig. 5.

III. Reachable and Controllable Set Definitions

In this section a number of sets are defined to characterize the flight capability of an entry vehicle. These sets include feasible, reachable, and controllable sets. Reachable and controllable sets are concepts from systems theory (see for example [1]). The standard definitions are modified as needed for the entry guidance context. In preparation for defining the reachable and controllable sets, several other sets are first defined. Standard set notation $S = \{p \in A\text{: property}\}$, read "the set S is composed of all points p found in set A such that the property is satisfied," is used.

A. Basic Set Definition

As introduced in Eq. (1), the state representation $x = [r, \theta, \phi, V, \gamma, \psi]^T$ is used. The state x is assumed to take values in a set $\mathrm{X} \subset \Re^6$; X will be specified for the computations, but is left general here. The set $U(t)$ of admissible σ control profiles is defined by

$$U(t) = \{\sigma[0,t] \in C^2[0,t]\text{: } |\sigma(\tau)| \le \sigma_{\max}, |\dot{\sigma}(\tau)| \le \dot{\sigma}_{\max}, |\ddot{\sigma}(\tau)| \le \ddot{\sigma}_{\max},\ \forall\ \tau \in [0,t]\} \tag{8}$$

where the bank-angle profile for the time interval zero to t is denoted by $\sigma[0,t]$ and $C^2[0,t]$ denotes the set of continuous functions with continuous first and second derivatives on the interval $[0,t]$. $U(t)$ depends on the time duration t and the constant bounds $\sigma_{\max}$, $\dot{\sigma}_{\max}$, and $\ddot{\sigma}_{\max}$.

The solution to the equations of motion, Eq. (1), at time t for the initial condition $x(0) = x_0$, is expressed by the nonlinear transition map

$$x(t) \equiv T[t, x_0; \sigma[0,t]] \tag{9}$$

denoting the dependence of $x(t)$ on the elapsed time t, x_0, and the bank-angle profile. Because the dynamics are time independent, the initial time is always taken to be zero, without loss of generality. The transition map also depends on the particular force models employed, but because the impact of modeling errors is not investigated in this paper, the notation does not explicitly indicate the model dependence. The state trajectory for time interval $[0,t]$ is expressed by

$$x[0,t] \equiv \bigcup_{0 \le \tau \le t} T[\tau, x_0; \sigma[0,\tau]] \tag{10}$$

Thus $x(t)$ denotes the value of x at time t, whereas $x[0,t]$ denotes the trajectory segment for the given time interval, a slight abuse of notation.

Let $P \subset \mathrm{X}$ denote the set of states that do not violate the path constraints, defined by

$$P = \{x \in \mathrm{X}\text{: } p(x) \le 0\} \tag{11}$$

where $p(x)$ is a vector that can include components specifying the limits on heat rate, acceleration, and dynamic pressure, for instance. The deployment set $\Delta \subset \mathrm{X}$, the set of acceptable parachute-deployment states, is defined by

$$\Delta = \{x \in \mathrm{X}\text{: } d(x) \le 0\} \tag{12}$$

where $d(x)$ is a vector specifying the inequality deployment constraints. The definition of $d(x)$ would, for example, include the limits shown in Fig. 5 on the deployment Mach number, dynamic pressure, and altitude. If the attention is on a particular (θ, ϕ) pair, then the deployment state is further restricted to $\Delta|_{(\theta,\phi)} = \{x \in \Delta\text{: } \Pi(x) = [\theta,\phi]^T\}$, where $\Pi(x) = Cx$ is the mapping that extracts the longitude and latitude state variables from the state vector x, with

$$C = \begin{bmatrix} 0 & 1 & 0 & 0 & 0 & 0 \\ 0 & 0 & 1 & 0 & 0 & 0 \end{bmatrix}$$

The initial entry states are limited to a subset $\mathrm{X}_0 \subset \mathrm{X}$, which may restrict the initial values of certain state variables. For instance, traditionally, the entry altitude is fixed at a given h_0, $\gamma_0 < 0$, and the range of initial speeds and heading angles to be considered may be specified, since these values are dictated by the approach trajectory and associated errors. For the reachable set, X_0 will have a single entry state.

Given an initial state $x_0 \in \mathrm{X}_0$, $(\sigma[0,t_f], x[0,t_f])$ is a feasible control-trajectory pair with final time $t_f > 0$, if it satisfies the conditions:

1) $\sigma[0,t_f] \in U(t_f)$.
2) $x(t) = T[t, x_0; \sigma[0,t]] \in P,\ \forall\ t \in [0,t_f]$.
3) $x(t_f) = T[t_f, x_0; \sigma[0,t_f]] \in \Delta$.

Let $F(\mathrm{X}_0, \mathrm{X}_f)$ denote the set of all feasible control-trajectory pairs with initial state in X_0 and final state in X_f, where X_f is Δ or the more restrictive $\Delta|_{(\theta,\phi)}$, depending on the situation.

B. Reachable Set

The reachable set $\mathrm{RS}(x_0) \subset \Delta$ is the set of deployment states corresponding to feasible control-trajectory pairs with entry state x_0, that is,

$$\mathrm{RS}(x_0) = \{x_f \in \Delta\text{: } \exists t_f \text{ and } (\sigma[0,t_f], x[0,t_f]) \in F(\{x_0\}, \Delta) \text{ with } x(t_f) = x_f\} \tag{13}$$

The symbol $\exists$ denotes *there exists*. In words, each final state in $\mathrm{RS}(x_0)$ can be reached by a feasible control-trajectory pair from x_0 for some t_f, where t_f may be different for each final state. The RFP is derived from $\mathrm{RS}(x_0)$ as follows:

$$\mathrm{RFP}(x_0) = \{[\theta,\phi]^T\text{: } \exists x_f \in \mathrm{RS}(x_0) \text{ with } \Pi(x_f) = [\theta,\phi]^T\} \tag{14}$$

Thus, to each value of $[\theta,\phi]^T \in \mathrm{RFP}(x_0)$, there corresponds at least one value of $x_f \in \mathrm{RS}(x_0)$.

C. Optimal Subset of the Reachable Set

There is typically more than one feasible control-trajectory pair that leads to a given $[\theta_f, \phi_f]^T \in \mathrm{RFP}(x_0)$; i.e., the set $F(\{x_0\}, \Delta|_{(\theta_f,\phi_f)})$ typically has more than one feasible control-trajectory pair. Rather than compute all the control-trajectory pairs that lead to a given (θ_f, ϕ_f), it is prudent to first decide which are of most interest and compute only those. Determining extremal points in F and RS is a means of characterizing these sets.

Using a cost function of the form

$$J(\sigma[0,t_f], x[0,t_f]) = f_0(x(0)) + f_F(x(t_f)) + \int_0^{t_f} f_L(x(\tau), \sigma(\tau))\, \mathrm{d}\tau \tag{15}$$

with Mayer terms, $f_0(x(0))$ and $f_F(x(t_f))$, and Lagrange term f_L, the trajectory that minimizes J is determined for each longitude–latitude pair (θ, ϕ) in $\mathrm{RFP}(x_0)$ over the set $F(\{x_0\}, \Delta|_{(\theta,\phi)})$, in order to obtain optimal subsets of $F(\{x_0\}, \Delta)$ and $\mathrm{RS}(x_0)$ denoted by $F^J(\{x_0\}, \Delta)$ and $\mathrm{RS}^J(x_0)$ and defined as

$$F^J(\{x_0\}, \Delta) = \bigcup_{[\theta,\phi]^T \in \mathrm{RFP}(x_0)} F^J(\{x_0\}, \Delta|_{(\theta,\phi)}) \tag{16}$$

where

$$F^J(\{x_0\}, \Delta|_{(\theta,\phi)}) = \{(\sigma[0, t_f], x[0, t_f]) \in F(\{x_0\}, \Delta|_{(\theta,\phi)})\text{: } J(\sigma[0, t_f], x[0, t_f]) \text{ is min over } F(\{x_0\}, \Delta|_{(\theta,\phi)})\} \quad (17)$$

and

$$\mathrm{RS}^J(x_0) = \{x_f \in \mathrm{RS}(x_0)\text{: } \exists t_f \text{ and } (\sigma[0, t_f], x[0, t_f]) \in F^J(\{x_0\}, \Delta) \text{ with } x(t_f) = x_f\} \quad (18)$$

Note that the minimization in Eq. (17) is with a free final time.

At a boundary point (θ, ϕ) of $\mathrm{RFP}(x_0)$, $F(\{x_0\}, \Delta|_{(\theta,\phi)})$ will typically have only one control-trajectory pair, but by default it minimizes J over $F(\{x_0\}, \Delta|_{(\theta,\phi)})$. Though a formal proof is not provided, it is clear that $\mathrm{RFP}^J(x_0) = \{[\theta, \phi]^T\text{: } \exists x_f \in \mathrm{RS}^J(x_0) \text{ with } \Pi(x_f) = [\theta, \phi]^T\}$ is equivalent to $\mathrm{RFP}(x_0)$.

D. Controllable Set

The controllable set $\mathrm{CS}(\theta_f, \phi_f) \subseteq \mathrm{X}_0$ is the set of entry states from which there exist a feasible trajectories to the longitude–latitude pair (θ_f, ϕ_f), and it is given by

$$\mathrm{CS}(\theta_f, \phi_f) = \{x_0 \in \mathrm{X}_0\text{: } \exists t_f \text{ and } (\sigma[0, t_f], x[0, t_f]) \in F(\mathrm{X}_0, \Delta|_{(\theta_f,\phi_f)}) \text{ with } x(0) = x_0\} \quad (19)$$

The controllable set footprint is derived from the $\mathrm{CS}(\theta_f, \phi_f)$ as follows:

$$\mathrm{CFP}(\theta_f, \phi_f) = \{[\theta_0, \phi_0]^T\text{: } \exists x_0 \in \mathrm{CS}(\theta_f, \phi_f) \text{ with } \Pi(x_0) = [\theta_0, \phi_0]^T\} \quad (20)$$

For each value of $[\theta_0, \phi_0]^T \in \mathrm{CFP}(\theta_f, \phi_f)$, there corresponds at least one value of $x_0 \in \mathrm{CS}(\theta_f, \phi_f)$. Note that this is a footprint (area on the (θ, ϕ) plane) of feasible entry points, not a landing footprint.

E. Optimal Subset of the Controllable Set

Analogous to the reachable set case, there is typically more than one feasible control-trajectory pair for a given $[\theta_0, \phi_0]^T \in \mathrm{CFP}(\theta_f, \phi_f)$; i.e., the set $F(\mathrm{X}_0|_{(\theta_0,\phi_0)}, \Delta|_{(\theta_f,\phi_f)})$ typically has more than one element. Trajectories are determined that minimize the cost function J shown in Eq. (15) for each longitude–latitude pair in $\mathrm{CFP}(\theta_f, \phi_f)$ and obtain optimal subsets of $F(\mathrm{X}_0, \Delta|_{(\theta_f,\phi_f)})$ and $\mathrm{CS}(\theta_f, \phi_f)$ denoted by $F^J(\mathrm{X}_0, \Delta|_{(\theta_f,\phi_f)})$ and $\mathrm{CS}^J(\theta_f, \phi_f)$ and defined as

$$F^J(\mathrm{X}_0, \Delta|_{(\theta_f,\phi_f)}) = \bigcup_{[\theta_0,\phi_0]^T \in \mathrm{CFP}(\theta_f,\phi_f)} F^J(\mathrm{X}_0|_{(\theta_0,\phi_0)}, \Delta|_{(\theta_f,\phi_f)}) \quad (21)$$

where

$$F^J(\mathrm{X}_0|_{(\theta_0,\phi_0)}, \Delta|_{(\theta_f,\phi_f)}) = \{(\sigma[0, t_f], x[0, t_f]) \in F(\mathrm{X}_0|_{(\theta_0,\phi_0)}, \Delta|_{(\theta_f,\phi_f)})\text{: } J(\sigma[0, t_f], x[0, t_f]) \text{ min over } F(\mathrm{X}_0|_{(\theta_0,\phi_0)}, \Delta|_{(\theta_f,\phi_f)})\} \quad (22)$$

and

$$\mathrm{CS}^J(\theta_f, \phi_f) = \{x_0 \in \mathrm{CS}(\theta_f, \phi_f)\text{: } \exists(\sigma[0, t_f], x[0, t_f]) \in F^J(\mathrm{X}_0, \Delta|_{(\theta_f,\phi_f)}) \text{ with } x(0) = x_0\} \quad (23)$$

where the minimization in Eq. (22) is with free final time. It is claimed that $\mathrm{CFP}^J(\theta_f, \phi_f) = \{[\theta, \phi]^T\text{: } \exists x \in \mathrm{CS}^J(\theta_f, \phi_f)$ with $\Pi(x) = [\theta, \phi]^T\}$ is equivalent to $\mathrm{CFP}(\theta_f, \phi_f)$.

IV. Reachable Set Computation and Applications

The trajectories presented in this and the next section have been obtained using the graphical environment for simulation and optimization (GESOP) [13], a trajectory-optimization program that provides several optimization methods. The optimization method CAMTOS [14], which includes two discretization options, direct multiple shooting and direct collocation, is used. A two-step strategy was used: direct collocation to obtain the initial guess, then direct multiple shooting to converge to an accurate solution.

A. Computational Approach

The optimal subset of the reachable set $\mathrm{RS}^J(x_0)$ is computed to study the trajectories with maximum deployment altitude and control authority. The $\mathrm{RFP}(x_0)$ is obtained from $\mathrm{RS}^J(x_0)$. The optimal trajectories that form $\mathrm{RS}^J(x_0)$ are computed using GESOP after defining the boundary, control and path constraints, and the cost function J. The final time t_f is free.

The entry state x_0 is shown in Table 3. Since the initial state is fixed, $\mathrm{X}_0 = \{x_0\}$. Table 3 also shows the minimum and maximum values of the state variables allowed during entry, defining the set X. No limits on heat rate, dynamic pressure, and acceleration are imposed, and hence P equals X. The values of these quantities will, however, be examined. The control constraints that define $U(t)$ are specified in Sec. II.C. Figure 5 shows the parachute-deployment constraints, which define the set Δ.

The trajectories are optimized to have high control authority and high deployment altitude by minimizing the cost function

$$J = k_\gamma[\gamma_f - \gamma(t_f)]^2 - k_h h(t_f) \quad (24)$$

where the positive constants k_γ and k_h are the weighting factors. For the two vehicles, the parameters used in the optimization are shown in Table 4. Limiting the maximum value of γ to an appropriately chosen upper bound $\gamma_{\max}$ is an effective way of limiting the lofting motion and increasing the control authority [8]. In [9] a term is included in the cost function to bring to zero the deployment flight-path angle, which decreases the lofting motion. In practice the vehicle control authority is never high enough to have a positive deployment flight-path angle. This term works better than including the Lagrange term $f_L = L\cos\gamma$ in the cost function [see Eq. (15)], which can provide undesirable results since lift is maximized when the altitude is minimized.

Optimal trajectories are computed for a grid of longitude–latitude pairs large enough to contain the RFP. The grid is established by first computing the maximum and minimum crossrange and downrange reachable from x_0. A uniform rectangular grid encompassing those extremal points is defined on the downrange–crossrange plane. The grid resolution used in the results presented is 10 km in downrange and 5 km in crossrange for the MSL-type vehicle and 10 km in downrange and 10 km in crossrange for the ellipsled. Then, with the trajectory final state constrained to the set $\Delta|_{(\theta,\phi)}$, where (θ, ϕ) corresponds to one of the downrange–crossrange pairs on the grid, the optimal trajectory is obtained. If a trajectory to a (θ, ϕ) pair is not feasible, the pair is outside the RFP and the trajectory is discarded.

Table 3 Entry state x_0

State variable	Initial value	Minimum value	Maximum value	Units
r	3522.2	r_p	3522.2	km
θ	−74.73192	−180	180	deg
ϕ	−43.7513	−90	90	deg
V	5433.5	0	5500	m/s
γ	−15.76793	−45	$\gamma_{\max}$	deg
ψ	15.634524	−90	90	deg

Table 4 Optimization parameters

Variable	Value	Units
k_γ	91.4	$1/\mathrm{deg}^2$
k_h	1.0	1/m
γ_f	0.0	deg
$\gamma_{\max}$	0.0	deg

Note that while scanning the crossrange points for a given downrange, it is not assumed that once a trajectory is found to be outside the RFP the remaining crossrange points are also outside the RFP. This allows, at the expense of extra computation, the obtaining of the lobes at low downranges visible in the following figures. With this approach the boundary of the RFP is estimated with a maximum error equivalent to the grid resolution.

The results obtained required extensive computation. The resolution of the grids was adjusted to have around 600 points for each set. Computations were carried out in a 2003-generation desktop PC, and on average each optimal trajectory took about three minutes. Hence, each set was obtained in about 30 hours.

B. Application to an MSL-Type Nominal Entry

The nominal RFP is shown in Fig. 6, with contours showing the deployment altitude. Note that *nominal* implies nominal entry state and nominal vehicle and planet models. The RFP is 175 km long in downrange and 90 km wide in crossrange. Figure 6 shows that near the boundary of the footprint the deployment altitudes are lowest. When all the control authority is used to minimize or maximize downrange, there is none left to raise deployment altitude. The interior of the RFP has the higher deployment altitudes, with the highest at downranges between 620 and 640 km. In Fig. 7 the deployment velocity contours are shown. For all the points inside the 470 m/s contour, the deployment velocity is the maximum allowed, Mach 2.2 or 484 m/s; this maximizes control authority. Most of the deployment points are placed at the right edge of the parachute box (Fig. 5).

Figure 8 shows the deployment dynamic pressure. Since the deployment velocity is the same for most of the RFP, the dynamic pressure looks like an inverted version of Fig. 6: low dynamic pressure for high deployment altitude and vice versa. Figure 9 shows the maximum heat rates achieved during the entry; for the shorter trajectories where the energy has to be dissipated in less time, the maximum heat rates are higher. Figure 10 shows the total heat load. Note that heat load follows a pattern roughly the reverse of the maximum heat rate.

All the points in the RFP(x_0) are, by definition, reachable from x_0. If a point had to be chosen within the RFP to be the nominal deployment target it can be inferred from Figs. 6–10 that the preferred area where the target should be placed is near the center of the RFP, where the maximum deployment altitude is the highest and the maximum heat rate and heat load are low. To quantitatively evaluate the best target point, one can define a scoring criterion. As an example, a scoring function, inspired by the approach in [15], is defined, based on the four criteria in Table 5. $h_{\min}$ and $h_{\max}$ are the minimum and maximum deployment altitudes found in RS^J; S_{hf} is one if $h(t_f) = h_{\max}$ and zero if $h(t_f) = h_{\min}$. It is desirable to have margins in the deployment conditions to account for trajectory tracking errors and to have flexibility to trigger the parachute deployment when the vehicle is over the target longitude and latitude. S_{dp} is maximum for deployment dynamic pressure equal to $\bar{q}_0$, the midpoint between $\bar{q}_{\min}$ and $\bar{q}_{\max}$; i.e., $\bar{q}_0 = 0.5(\bar{q}_{\min} + \bar{q}_{\max})$. W_{dp} is set to zero in the scoring of RS^J since it interferes with S_{hf}; however, it will be used for the scoring of CS^J. $\dot{Q}_{\max}$ is the maximum heat rate achieved during the trajectory; $(\dot{Q}_{\max})_{\max}$ and $(\dot{Q}_{\max})_{\min}$ are the maximum and minimum values of $\dot{Q}_{\max}$ for the trajectories that form

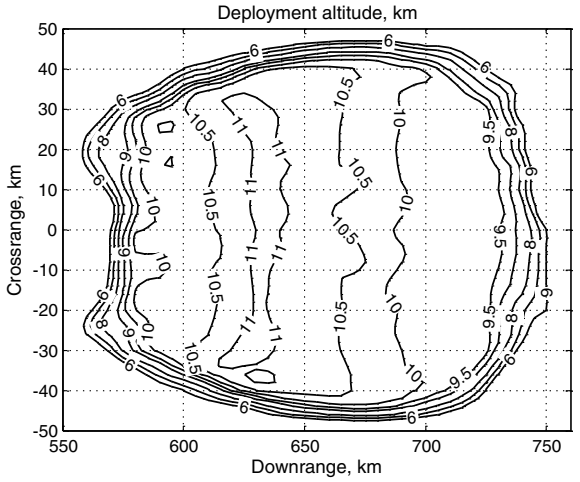

Fig. 6 Nominal RFP and deployment altitudes.

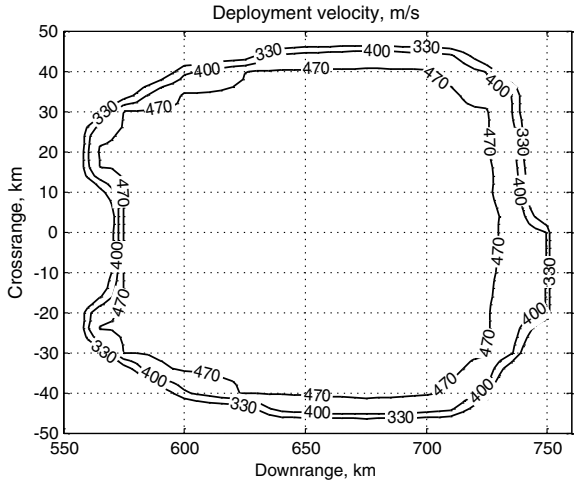

Fig. 7 RFP with deployment velocities.

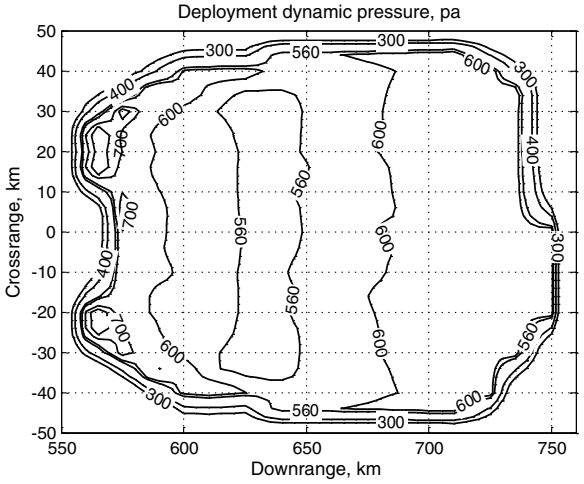

Fig. 8 Deployment dynamic pressure.

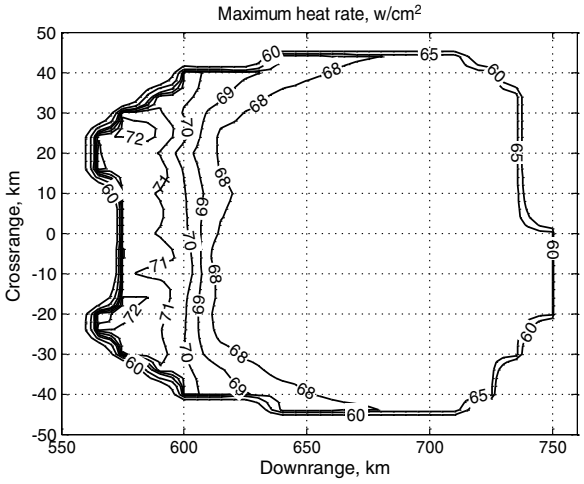

Fig. 9 Maximum heat rate.

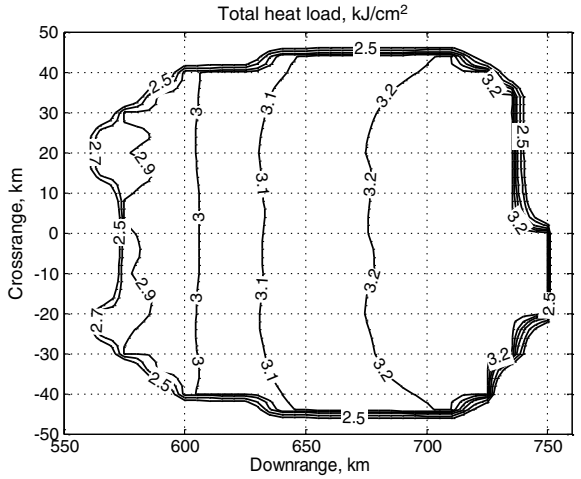

Fig. 10 Total heat load.

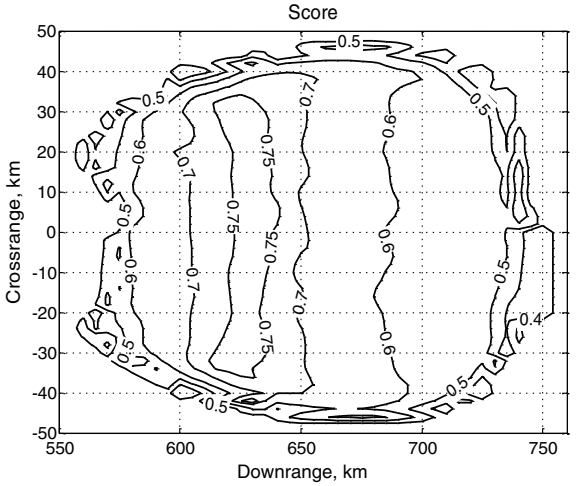

Fig. 11 Score.

RS^J; hence, S_{hr} is one when $\dot{Q}_{\max} = (\dot{Q}_{\max})_{\min}$ and zero when $\dot{Q}_{\max} = (\dot{Q}_{\max})_{\max}$. Q is the total heat load, and S_{hl} is one when Q equals the minimum heat rate for the trajectories that form RS^J and zero when it equals the maximum. With these definitions, the score S is calculated by adding up all the scores multiplied by the corresponding weight as follows:

$$S = W_{hf}S_{hf} + W_{dp}S_{dp} + W_{hr}S_{hr} + W_{hl}S_{hl} + W_{bs}S_{bs} \qquad (25)$$

With these definitions the score S is a number between zero and one provided that the weights add up to one. The score for the nominal MSL mission is shown in Fig. 11. The best area to place the nominal target point is between 600 and 650 km downrange and −20 and +20 km crossrange. The scoring function used in this paper is only an illustration; other choices might be more appropriate depending on the mission.

C. Application to an Ellipsled-Type Nominal Entry

The nominal RFP for the ellipsled vehicle is shown in Fig. 12 along with the nominal RFP for the MSL vehicle. The ellipsled RFP is 300 km long in downrange and 180 km wide in crossrange, significantly larger that the one achievable with the MSL vehicle. Results showing the same trend are presented in [3], where optimal landing footprints are calculated (under several simplifications) for vehicles with different L/Ds. Figure 13 shows the maximum deployment altitude. Comparing with Fig. 6, the ellipsled vehicle can reach higher deployment altitudes: 15.5 km compared with 11 km for the MSL configuration. Parachute deployment altitudes for different L/Ds are shown in [7].

Figure 14 shows the deployment dynamic pressure. The deployment dynamic pressures are as low as 350 Pa, compared with 550 Pa for the MSL vehicle (Fig. 8). Figure 15 shows the maximum heat rate achieved for each of the trajectories with final states in RS^J. The higher L/D of the ellipsled vehicle generates higher trajectories with lower atmospheric density and thus with lower heat rate (compared with Fig. 9).

Figure 16 shows the total heat load, which is roughly the reverse pattern shown in Fig. 15. Short trajectories have higher heat rate and lower heat load; long trajectories have lower heat rate and higher heat load. As with the maximum heat rate, the higher altitude trajectories of the ellipsled configuration provide a lower heat load compared with the MSL configuration (see Fig. 10). The scoring function is the same used for the MSL configuration shown in Table 5 and Eq. (25). The score distribution for the ellipsled is shown in Fig. 17.

Table 5 Scoring criteria

Score	Description	Weight	Formula
S_{hf}	Deployment altitude	$W_{hf} = 0.40$	$\frac{h(t_f)-h_{\min}}{h_{\max}-h_{\min}}$
S_{dp}	Deployment dynamic pressure	$W_{dp} = 0.00$	$1 - \frac{\lvert\bar{q}(t_f)-\bar{q}_0\rvert}{\bar{q}_{\max}-\bar{q}_0}$
S_{hr}	Maximum heat rate	$W_{hr} = 0.30$	$\frac{\dot{Q}_{\max}-(\dot{Q}_{\max})_{\max}}{(\dot{Q}_{\max})_{\min}-(\dot{Q}_{\max})_{\max}}$
S_{hl}	Total heat load	$W_{hl} = 0.30$	$\frac{Q-Q_{\max}}{Q_{\min}-Q_{\max}}$

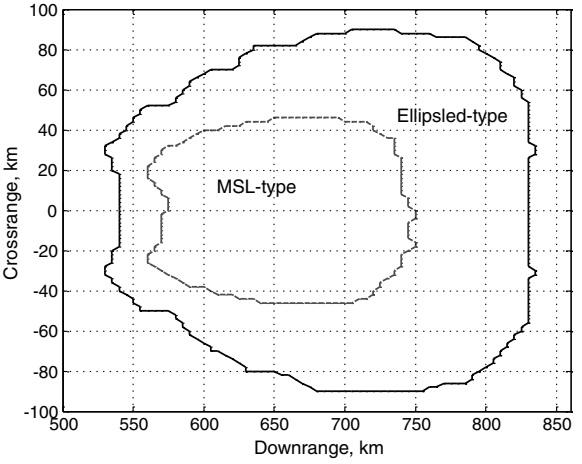

Fig. 12 Ellipsled vs MSL RFP.

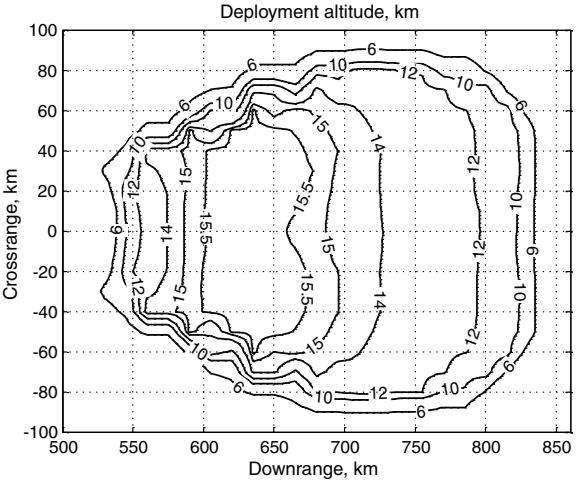

Fig. 13 Deployment altitude.

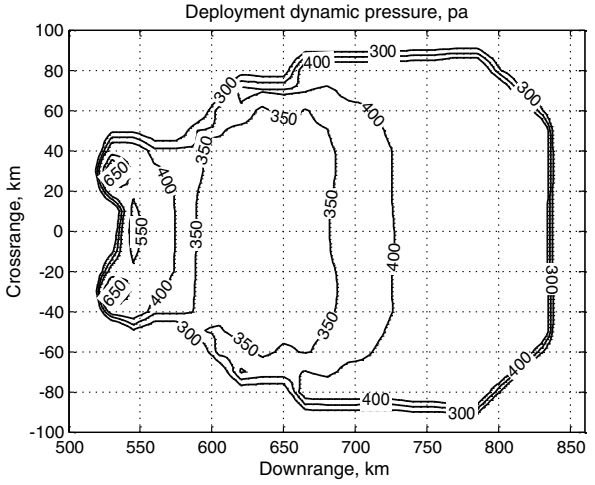

Fig. 14 Deployment dynamic pressure.

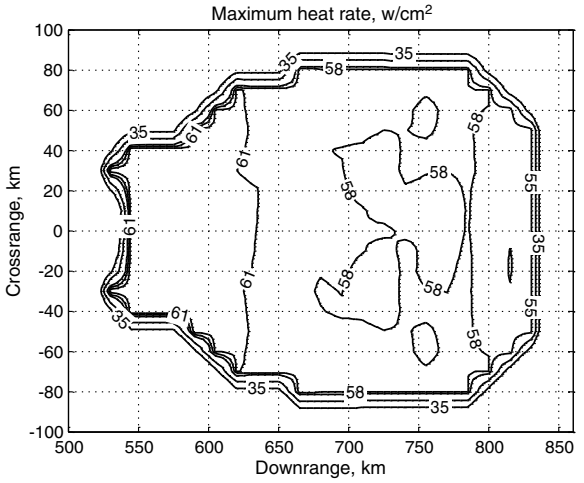

Fig. 15 Maximum heat rate.

V. Controllable Set Computation and Applications

A. Computational Approach

Similar to the strategy for the RS, an optimal subset of the controllable set, denoted $\mathrm{CS}^J(\theta_f, \phi_f)$, is computed along with the associated footprint $\mathrm{CFP}(\theta_f, \phi_f)$. The boundary constraints, the path constraints, the control constraints, and the cost function for the optimal control problem are first specified. Table 6 shows the entry

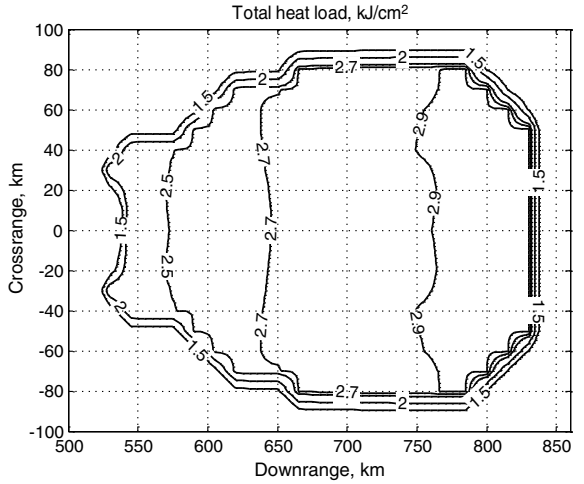

Fig. 16 Total heat load.

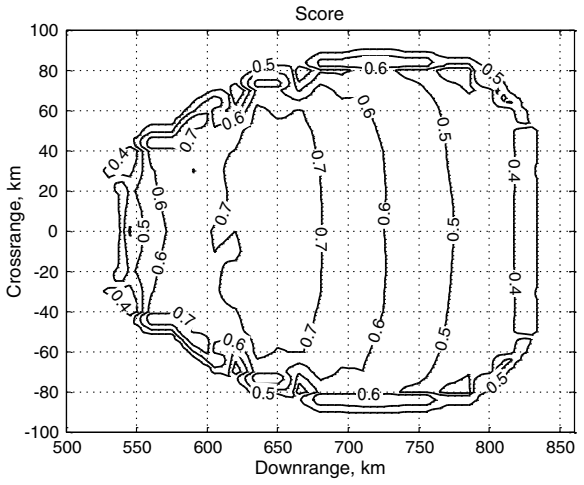

Fig. 17 Score.

boundary constraints for both the MSL-type and the ellipsled-type vehicles, which define X_0 in each case. Table 6 also shows the minimum and maximum values of the state variables allowed during entry, which define X in each case. These limits are never reached except for the one corresponding to maximum flight-path angle, which is constrained to a specified $\gamma_{\max}$ to ensure the vehicle has enough control authority by avoiding a lofting motion, as explained in Sec. II.A. No constraints on dynamic pressure, heat rate, heat load, and total acceleration are imposed, and hence $P = \mathrm{X}$. The values of these variables will, however, be examined. For all the trajectories, $\gamma_{\max} = 0$ deg. The deployment set Δ is defined in Fig. 5. The control constraints that define $U(t)$ are specified in Sec. II.C. The target pair (θ_f, ϕ_f) is set to $(\theta_f, \phi_f) = (-61.08, -40.0)$.

The variations in the initial heading angle ψ_0 are assumed to be caused by a deorbit timing error, and are thus associated with a lateral offset from the nominal entry point. The initial heading angle ψ_0 of each trajectory in CS^J matches the heading angle of a point on the great circle containing the nominal entry point and the target site (θ_f, ϕ_f). The particular point on this nominal great circle is the one whose perpendicular contains the entry point (θ_0, ϕ_0) as shown in Fig. 18. The initial radius is a fixed single value; the same value used for the computation of the RS. The initial velocity is fixed since for typical entry state dispersions its variation is small. This assumption is not necessary; the initial velocity can be varied at the expense of more computation.

The six-dimensional CS is viewed by projecting it along the other coordinate axes onto the (θ, ϕ) plane; this is the CFP. Then, the level sets for quantities of particular interest are superimposed on the CFP. For example, a more comprehensive characterization of the entry corridor is achieved by computing for each point $(\theta_0, \phi_0) \in \mathrm{CFP}$, the trajectories with the maximum and minimum flight-path angles. Thus the cost function is

$$J = k\gamma(0) \tag{26}$$

where k is one for minimum entry flight-path angle, and negative one for maximum entry flight-path angle. Note that minimum and maximum entry γ are equivalent to steepest and shallowest entry γ respectively. No term for increasing the control authority is included in the cost function, because it would compete with maximizing the

Table 6 Entry state and state constraints

State variable	Nominal entry value	Minimum value	Maximum value	Units
r	3522.2	r_p	3522.2	km
θ	θ_0	−180	180	deg
ϕ	ϕ_0	−90	90	deg
V	5433.5	0	5800	m/s
γ	Free	−45	$\gamma_{\max}$	deg
ψ	ψ_0	−90	90	deg

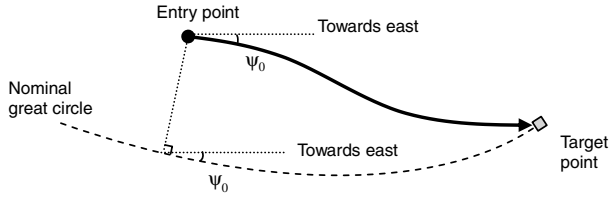

Fig. 18 Initial heading angle.

entry flight-path angle, since steep entries present higher control authority. Instead, the path constraint $\gamma < \gamma_{\max}$ is imposed.

The algorithm used to obtain the CS is equivalent to the one described in Sec. IV.A for the RS. Firstly, the maximum and minimum controllable downranges and crossranges are obtained. Then, a uniform rectangular grid containing those extremal values is defined on the downrange–crossrange plane. The grid resolution used for the computation of the CS is 50 km in downrange and 25 km in crossrange for both vehicles. Finally, for each of the grid points, the associated θ_0 and ϕ_0 are used to calculate the minimum and maximum entry flight-path-angle trajectories.

B. Application to an MSL-Type Entry

Continuing with the characterization of an MSL mission, CS^J is presented in this section. Figure 19 shows the CFP for the minimum entry flight-path-angle case, which has a size of 1200 km in downrange and an average of around 200 km in crossrange. An entry point at a downrange of 1200 km and a crossrange of 100 km means that from this entry point a vehicle has to fly 1200 km parallel to the nominal great circle and 100 km normal to it to reach the target landing site. The nominal entry point used in the previous section (Table 3) corresponds to a downrange of 640 km and a crossrange of 0 km. The CFP is not symmetric due to Coriolis effects. Figure 20 shows the CFP with the maximum entry flight-path angles.

Shorter downranges require steeper entry flight-path angles, and longer downranges require shallower entry flight-path angles. Figure 21 shows the difference between the maximum and minimum entry flight-path angles, i.e., the depth of the CS^J, terminology used in [2,5,6]. The depth decreases as the boundary of CS^J is approached. Figure 22 shows the contours of maximum heat rate on the CFP for the steepest entry flight-path-angle case, and Fig. 23 shows the total heat load for the case of shallowest entry flight-path angle. Restricting attention to values of heat rate and heat load at the maximum and minimum entry flight-path-angle values is based on the assumption that the extremal values of those quantities occur there. In [16], approximate formulas for lifting entry with constant $\sigma = 0$ show that the maximum heat rate increases as the entry angle steepens and that the total heat load increases as the entry angle becomes shallower. In a controlled entry with nonconstant σ, it is assumed that these tendencies are still valid. Figure 22 shows that the maximum heat rate is increasing for steeper entry flight-path angles and lower downranges. If the maximum heat rate is limited to a certain value the minimum entry flight-path angle and the minimum downrange would be constrained.

Figure 23 shows the total heat load for the maximum entry flight-path-angle case, in which the heat loads are higher than for the minimum flight-path-angle case. The pattern is roughly the reverse

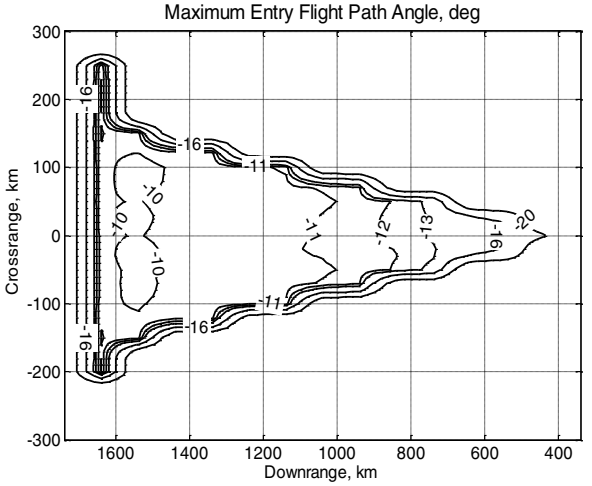

Fig. 20 CFP for maximum flight-path angle.

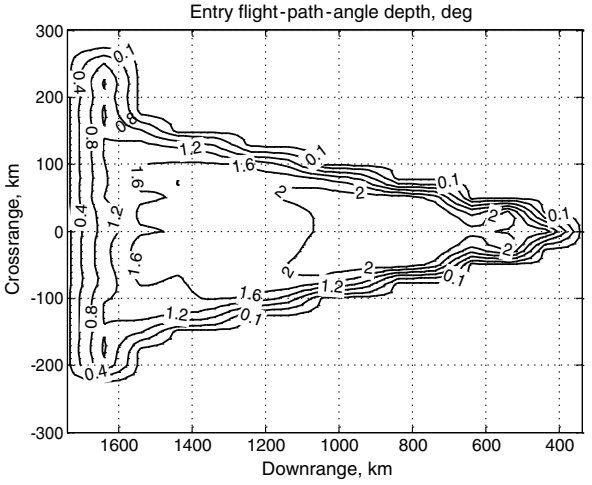

Fig. 21 Entry flight-path-angle depth.

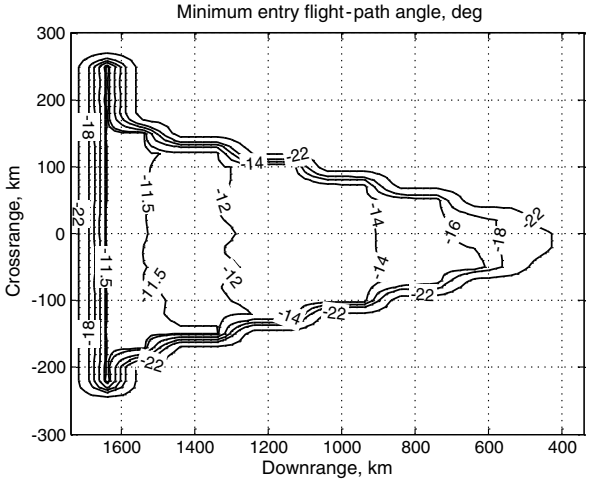

Fig. 19 CFP for minimum entry flight-path angle.

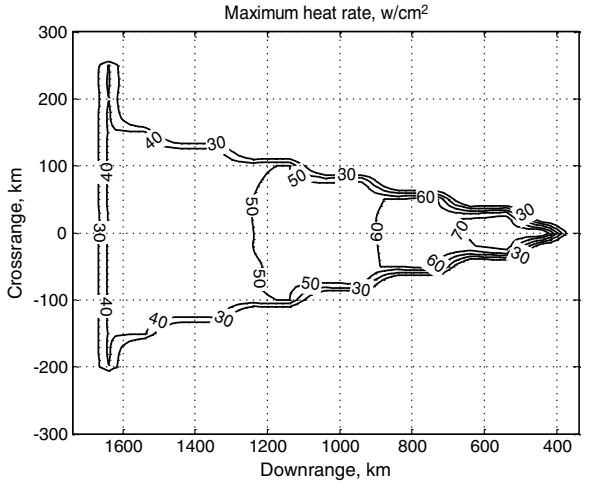

Fig. 22 Maximum heat rate [minimum $\gamma(0)$ case].

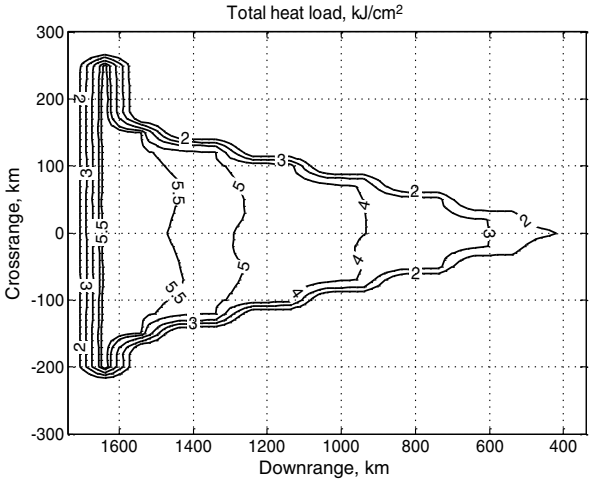

Fig. 23 Heat load [maximum $\gamma(0)$ case].

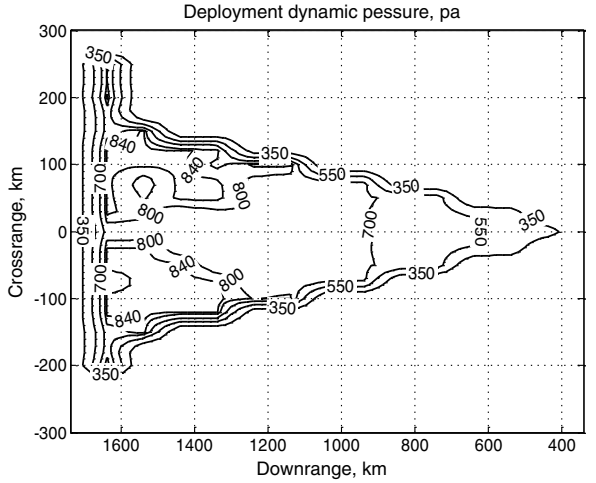

Fig. 24 Deployment dynamic pressure [minimum $\gamma(0)$ case].

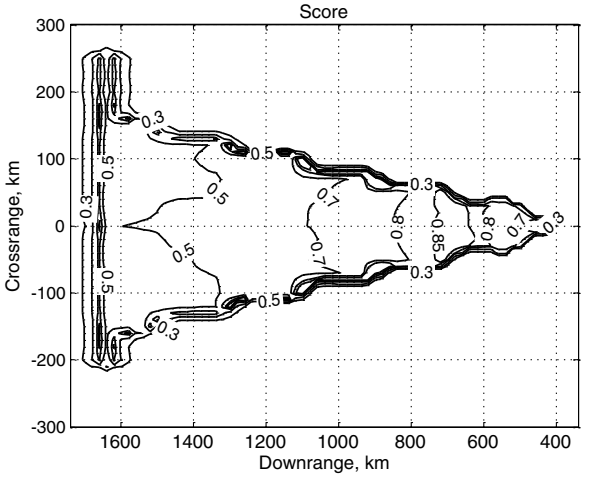

Fig. 26 Score [minimum $\gamma(0)$ case].

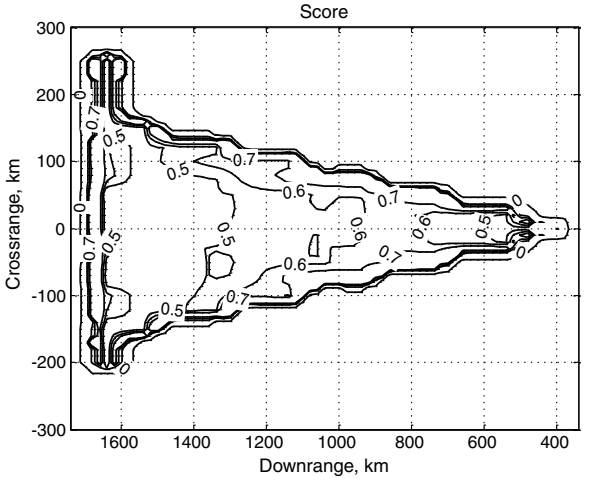

Fig. 27 Score [maximum $\gamma(0)$ case].

of the one for maximum heat rate: heat load is maximum where heat rate is minimum and vice versa.

Figures 24 and 25 show the deployment dynamic pressure for the minimum and maximum entry flight-path-angle cases, respectively. The deployment altitude for all the trajectories is very close to the minimum 6 km (this allows for the optimization of the entry flight-path angle), and hence the deployment dynamic pressure is an indication of the deployment velocity. Trajectories with shallow entry flight-path angle have a higher deployment velocity and dynamic pressure than trajectories with steep entry flight-path angles.

The scoring function used for the CS is the one used for the RS [Eq. (25)], with $W_{hf} = 0$, $W_{hr} = 0.333$, $W_{hl} = 0.333$, and $W_{dp} = 0.333$. Figures 26 and 27 show the score map for the minimum and maximum entry flight-path-angle cases. The scores are higher for steeper entry flight-path angles at a given entry point. Figure 28 shows the entry maximum and minimum entry flight-path angles along the

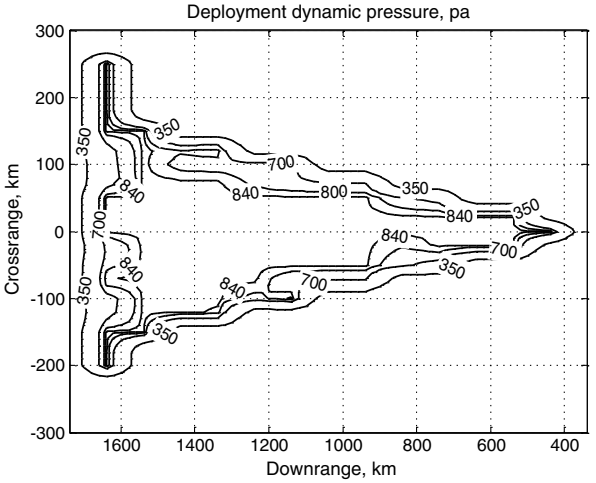

Fig. 25 Deployment dynamic pressure [maximum $\gamma(0)$ case].

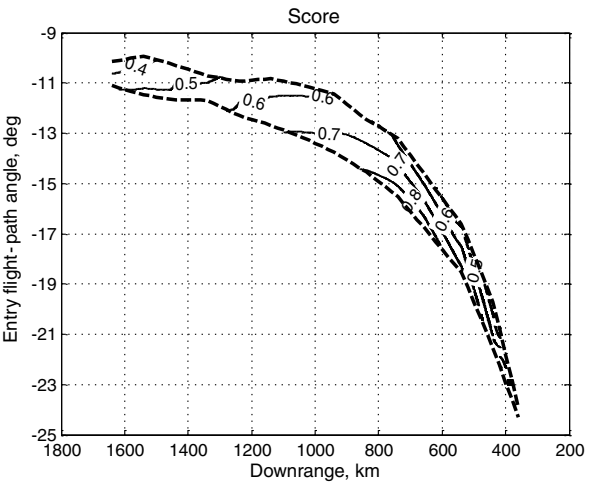

Fig. 28 Score (zero crossrange).

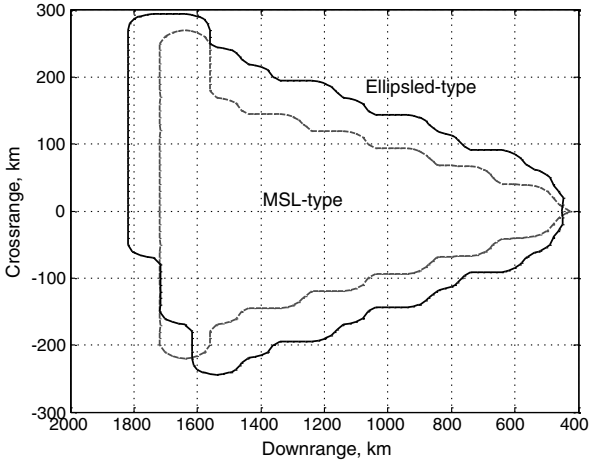

Fig. 29 CFP MSL vs ellipsled.

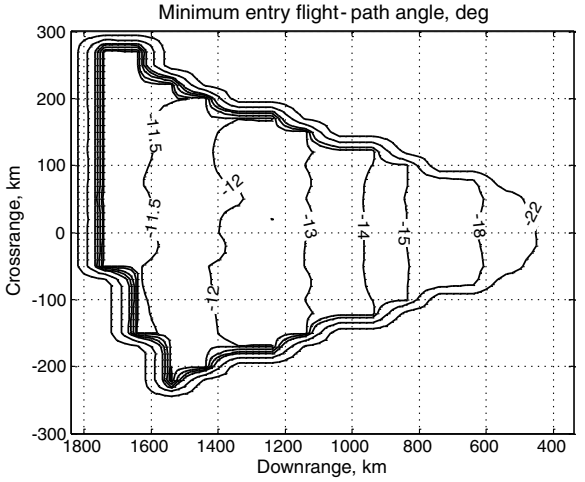

Fig. 30 CFP for minimum entry flight-path angle.

line of zero crossrange with the score level sets, which have been linearly interpolated between the two surfaces. According to the scoring function, the best places for the entry point are between 600 and 800 km downrange and as close to the steepest allowable entry flight-path angle as possible. Of course, if modeling errors and the need for control margin and approach navigation accuracy are taken into account, the steepest entry angle would not be chosen.

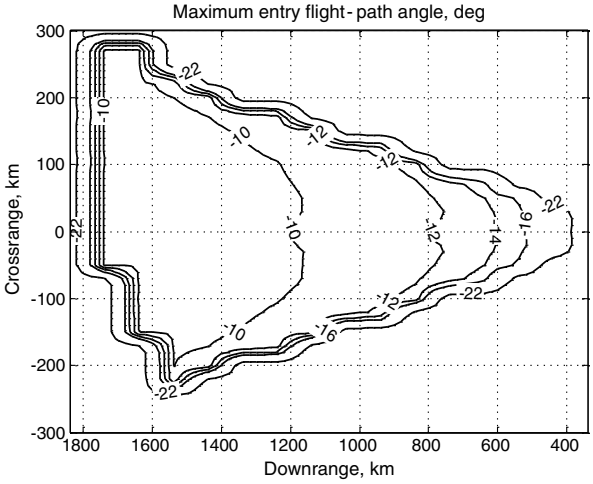

Fig. 31 CFP for maximum entry flight-path angle.

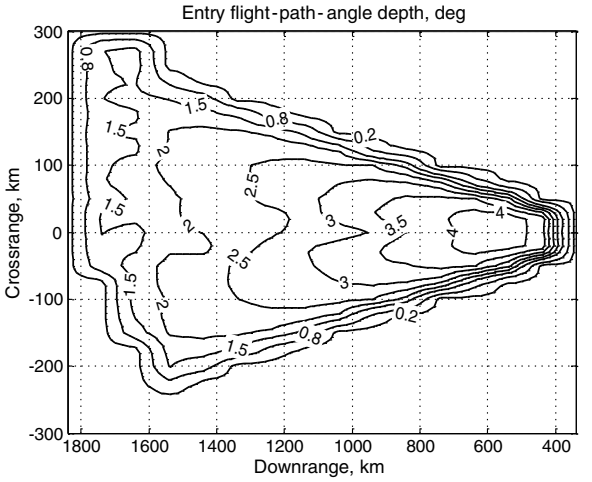

Fig. 32 Entry flight-path-angle depth.

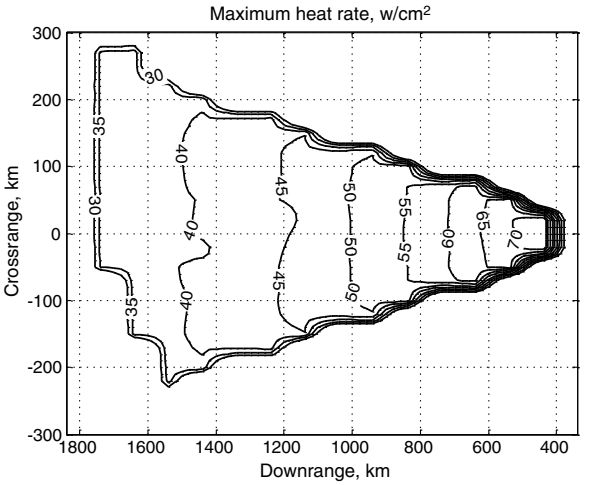

Fig. 33 Maximum heat rate [minimum $\gamma(0)$ case].

C. Application to an Ellipsled-Type Vehicle

The CFPs for the MSL-type and ellipsled vehicles are compared in Fig. 29. The increase L/D of the ellipsled allows mainly for more crossrange. The dimensions of the ellipsled CFP are 1300 km in downrange and around 300 km in crossrange on average. For the ellipsled, Fig. 30 shows the minimum flight-path angle and Fig. 31 the maximum flight-path angle.

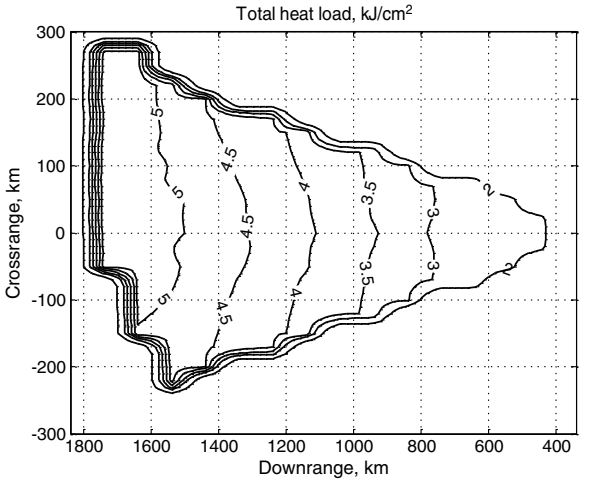

Fig. 34 Heat load [maximum $\gamma(0)$ case].

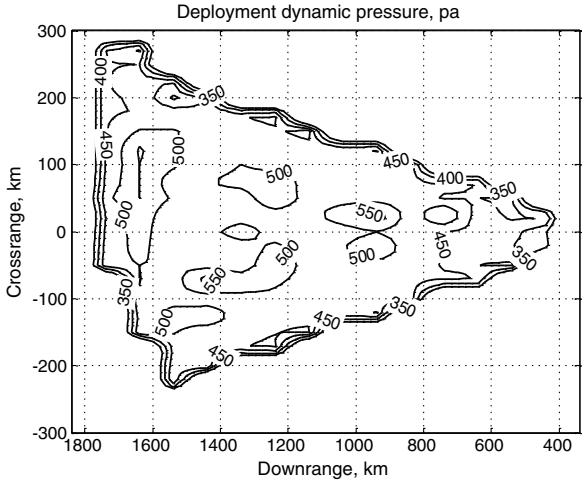

Fig. 35 Dynamic pressure [minimum $\gamma(0)$ case].

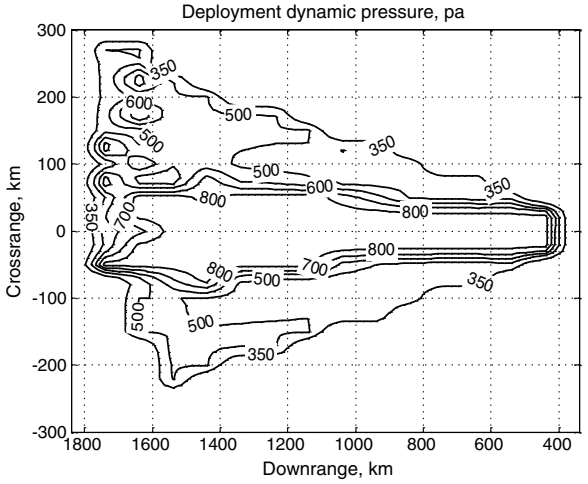

Fig. 36 Dynamic pressure [maximum $\gamma(0)$ case].

Compared with the MSL-type vehicle, the ellipsled can accommodate a wider range of entry flight-path angles for trajectories with the same downrange. This can be seen in Fig. 32: a 4 deg variation in flight-path angle can be accommodated by the ellipsled. An MSL-type vehicle can accommodate a variation of 2 deg.

The higher-altitude trajectories of the ellipsled vehicle have lower heat rates and heat loads than trajectories flown by the MSL-type vehicle for the same downranges. Maximum heat rate is depicted in Fig. 33; heat load is shown in Fig. 34. Figures 35 and 36 show the deployment dynamic pressure. As with the MSL-type vehicle, the deployment altitude is very close to the minimum allowed, so dynamic pressure is indicative of the deployment velocity. The deployment dynamic pressure is higher for shallower entry flight-path angles.

Scoring maps are calculated with the same weights used for the MSL vehicle CS. The score is higher for steeper entry flight-path

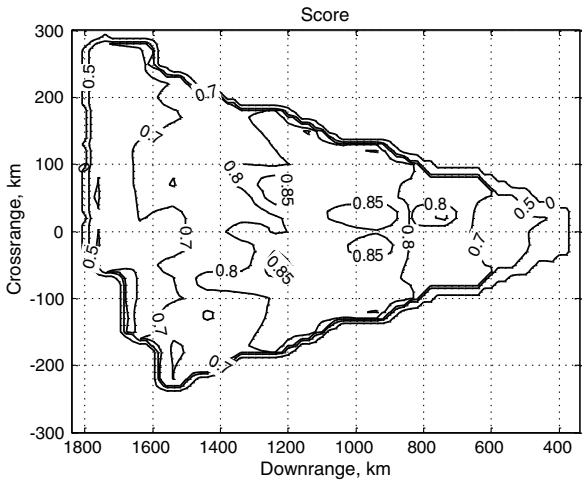

Fig. 37 Score [minimum $\gamma(0)$ case].

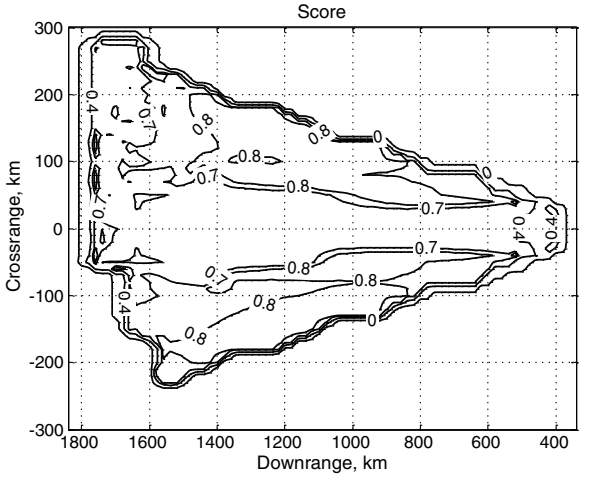

Fig. 38 Score [maximum $\gamma(0)$ case].

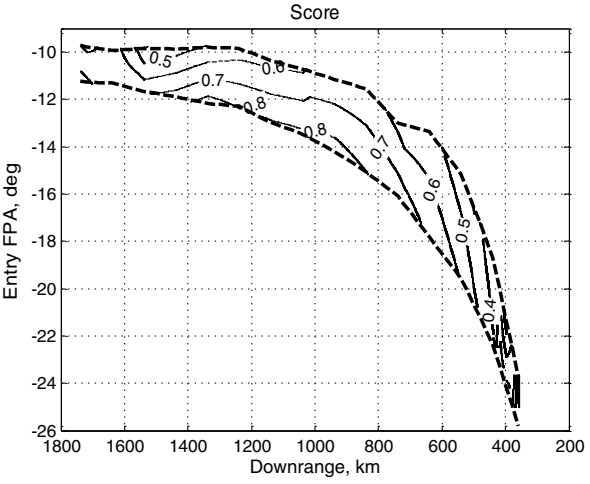

Fig. 39 Score (zero crossrange).

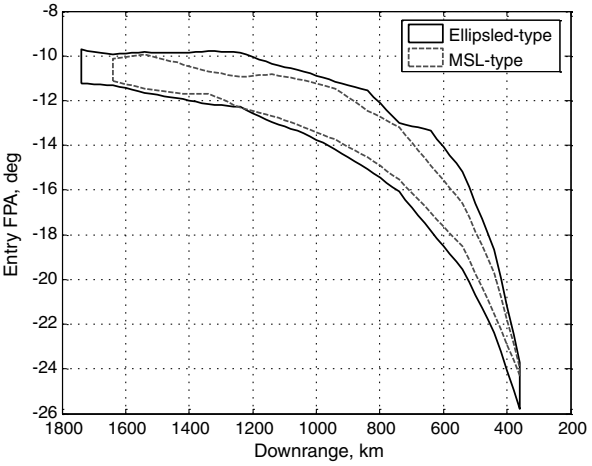

Fig. 40 Entry flight-path-angle depth comparison (zero crossrange).

angles, as seen in Figs. 37 and 38. Maximum and minimum entry flight-path angle along the zero crossrange line and the level set of the scores are shown in Fig. 39. It can be seen that the best area to place the entry state, for zero crossrange, is between 800 and 1400 km and the steepest entry flight-path angle.

Figure 40 presents a comparison between the acceptable entry flight-path angles along the zero crossrange line, showing that the vehicle with higher L/D can accommodate a wider range of entry flight-path angles. A direct relation between L/D and entry flight-path-angle depth is also shown in [6].

VI. Discussion

A. L/D Effect

Higher L/D provides a larger RFP (see Fig. 12); i.e., more landing sites are reachable from a given entry point.

An increase in L/D enlarges the CS (see Figs. 29 and 40); i.e., there are more feasible entry states for a given deployment location. Higher L/D especially allows for a wider range of entry flight-path angles. Note that the freedom in the entry flight-path angle diminishes the differences in size between the CFPs of the MSL vehicle and the ellipsled vehicle, as opposed to the RFP, where the differences are significant. Hence, with higher L/D there is more capability to accommodate entry state, atmospheric, and aerodynamic dispersions. An increase in L/D also allows higher deployment altitude and lower deployment dynamic pressure, maximum heat rate, and heat load.

B. Entry Guidance Algorithm Evaluation

For guidance algorithms that combine a trajectory planner and a trajectory tracker (e.g., [17]), the reachable and controllable sets can be used to assess the performance of the trajectory planner. Because the boundaries of the RS are achieved by minimizing or maximizing a function of the final state variables, e.g., downrange or crossrange, any planner that is not solving these trajectory-optimization problems will only be capable of planning trajectories to an interior subset of the RS. How large this subset is relative to the RS is the measure of the capability of the planning algorithm. Reference [4] shows a comparison of landing footprints obtained with a trajectory planner and by optimization. Similarly, the CS can be used to evaluate a trajectory planner. The set of entry states from which a planner can construct a trajectory to a designated landing site can be obtained. This set will be a subset of the CS, and it can be compared with the CS to evaluate the capabilities of the planning algorithm.

The evaluation of the planner will depend on the design objectives. In some cases it is desirable for the planner to cover as much of the RS and CS as possible so that large dispersions can be accommodated. In other cases, coverage may not be as important as other capabilities such as planning trajectories with high control authority and high deployment altitude.

C. Nominal Entry Point and Landing Site Selection

The RS can be used to decide the best nominal target site for a given entry state and baseline planet and vehicle models. A scoring function, a weighted sum of several criteria, can identify the best area for the landing site. Using the scoring function and weights shown in Sec. IV.B, there is an area at around 625 km downrange and 0 km crossrange where the landing site can be chosen for best overall performance for both configurations (compare Figs. 11 and 17).

When the landing site is given, the CS can be used, via the computation of a scoring function, to select a nominal entry state. The scoring function and weights used in this paper are only illustrative. The approach navigation control accuracy should also be compared with the CS size for the selection of the nominal entry state; the potential dispersions of the nominal entry state should fit in the CS. For instance, MSL has an expected 3σ entry flight-path-angle uncertainty dispersion of ± 0.20 deg [18]; this value, compared with the values shown in Fig. 21, indicates that approach navigation accuracy does not significantly reduce the area where the nominal entry state can be placed, since most of the CS has a depth greater than 0.4 deg. This application also highlights the utility of the CS for linking the entry phase to the approach phase.

D. Skip-Entry Planning

Although the examples in this paper were limited to Mars entry, reachable and controllable set analysis is applicable to entry at Earth and other atmosphere-bearing planets and satellites. For example, current plans for the new crew exploration vehicle, Orion, require delivering the crew safely to a designated landing site with high accuracy, without violating crew and vehicle constraints, from a large range of entry conditions [19]. In the case of a return from the moon, accommodating downranges from 3100 to 5400 nm requires skip-entry trajectories. The controllable set for a designated landing site can be used to evaluate the capability of an entry guidance algorithm to meet the downrange requirements. Additionally, the computation of the reachable set for the skip phase alone may be of interest. The skip reachable set can then be compared with the (second) entry controllable set to determine the set of states that are both reachable via a skip trajectory and controllable to the landing site. The use of reachable and controllable sets for skip-entry trajectories is addressed in more detail in [20].

E. Computational Requirements

Reachable and controllable sets could be useful for an onboard flight-management system. They could provide information for landing site selection, deorbit planning, or skip-entry planning. For onboard use, it would be necessary to develop a less computationally intensive approach than was used for this paper. There are many potential means of reducing the computation that could be explored, such as reducing the resolution and reducing the accuracy via various approximations. As an example, a computationally simpler approach for determining landing footprints is described in [4].

VII. Conclusions

Analysis of the reachable and controllable sets and the related reachable and controllable set footprints is a means of characterizing the performance of an entry vehicle. As an example, the sets were used to characterize the performance of two vehicle configurations for Mars entry with special attention to the effect of lift-to-drag ratio on parachute-deployment altitude, heating, and the entry corridor. Reachable and controllable set analysis can also be used to select a nominal entry state or a nominal landing site, to assess trajectory planners for guidance, and to plan skip-entry trajectories.

Acknowledgment

The research reported in this paper was sponsored by the Jet Propulsion Laboratory, California Institute of Technology, under contract with the National Aeronautics and Space Administration.

References

[1] Sontag, E. D., *Mathematical Control Theory*, 2nd ed., Springer, New York, 1998.

[2] Wingrove, R. C., "A Study of Guidance to Reference Trajectories for Lifting Reentry at Supercircular Velocity," NASA TR-R-151, Ames Research Center, Moffet Field, CA, Dec. 1963.

[3] Vinh, N. X., *Optimal Trajectories in Atmospheric Flight*, Elsevier, New York, 1981.

[4] Saraf, A., Leavitt, J. A., Ferch, M., and Mease, K. D., "Landing Footprint Computation for Entry Vehicles," AIAA Paper 2004-4774, Aug. 2004.

[5] Carroll, F., Zvara, J., Black, A., Blatt, P., Bohling, R., Burke, M., Kanter, J., Lickly, D., Morth, R., Rosamond, D., and Wingrove, R., "Guidance and Navigation for Entry Vehicles," NASA SP-8015, Nov. 1968.

[6] Wong, T. J., and Slye, R. E., "The Effect of Lift on Entry Corridor Depth and Guidance Requirements for the Return Lunar Flight," NASA TR-R-80, Ames Research Center, Moffett Field, CA, 1961.

[7] Braun, R. D., and Manning, R. M., "Mars Exploration Entry, Descent, and Landing Challenges," *Journal of Spacecraft and Rockets*, Vol. 44, No. 2, 2007, pp. 310–323. doi:10.2514/1.25116

[8] Benito, J., and Mease, K., "Entry Trajectory Planning for Higher Elevation Landing," *AAS/AIAA Astrodynamics Specialist Conference*, AAS Paper 07-309, Mackinac Island, MI, Aug. 2007.

[9] Boada, J., Benito, J., and Mease, K., "Near Optimal Planner for Higher Elevation Landing," *2008 Pegasus–AIAA Student Conference*, Prague, Czech Republic.

[10] Masciarelli, J. P., Westhelle, C. H., and Graves, C. A., "Aerocapture Guidance Performance for the Neptune Orbiter," *AIAA Atmospheric Flight Mechanics Conference*, AIAA Paper 2004-4954, Providence, RI, Aug. 2004.

[11] Lockwood, M. K., Sutton, K., Prabhu, R., and Powell, R. W., "Entry Configurations and Performance Comparisons for the Mars Smart Lander," *AIAA Atmospheric Flight Mechanics Conference*, AIAA Paper 2002-4407, Monterey, CA, Aug. 2002.

[12] Sutton, K., and Graves, R., "A General Stagnation-Point Convective-Heating Equation for Arbitrary Gas Mixtures," NASA TR R-376, 1971.

[13] GESOP: Graphical Environment for Simulation and Optimization, Ver. 4.7.0, Astos Solutions, Germany, http://www.astos.de/.

[14] Gath, P. F., "CAMTOS: A Software Suite Combining Direct and Indirect Trajectory Optimization Methods," Ph.D. Thesis, Univ. of Stuttgart, Stuttgart, Germany, Nov. 2002.

[15] Hanson, J., and Jones, R., "Test Results for Entry Guidance Methods for Space Vehicles," *Journal of Guidance, Control, and Dynamics*, Vol. 27, No. 6, 2004, pp. 960–966. doi:10.2514/1.10886

[16] Loh, W. H. T., *Re-Entry and Planetary Entry Physics and Technology*, Vol. 1, Springer–Verlag, New York, 1968.

[17] Saraf, A., Leavitt, J. A., Chen, D. T., and Mease, K. D., "Design and Evaluation of an Acceleration Guidance Algorithm for Entry," *Journal of Spacecraft and Rockets*, Vol. 41, No. 6, 2004, pp. 986–996. doi:10.2514/1.11015

[18] Wolf, A., Tooley, J., Ploen, S., Ivanov, M., Acikmese, B., and Gromov, K., "Performance Trades for Mars Pinpoint Landing," *2006 IEEE Aerospace Conference*, Big Sky, MT, March 2006.

[19] Broome, J., and Johnson, W., "Orion Entry, Descent, and Landing Performance and Mission Design," *AIAA Guidance, Navigation and Control Conference and Exhibit*, AIAA Paper 2007-6430, Hilton Head, SC, Aug. 2007.

[20] Benito, J., and Mease, K., "Skip-Entry Trajectory Planning Based on Reachable and Controllable Sets," *20th AAS/AIAA Space Flight Mechanics Meeting*, AAS Paper 10-126, San Diego, CA, Feb. 2010.